Wang *et al. PhotoniX* (2022) 3:11
https://doi.org/10.1186/s43074-022-00058-0

PhotoniX

RESEARCH Open Access

# Flexible minimally invasive coherent anti-Stokes Raman spectroscopy (CARS) measurement method with tapered optical fiber probe for single-cell application

Tong Wang[1,2,3], Junfeng Jiang[1,2,3*], Kun Liu[1,2,3], Shuang Wang[1,2,3], Panpan Niu[1,2,3], Yize Liu[1,2,3] and Tiegen Liu[1,2,3]

*Correspondence:
jiangjfjxu@tju.edu.cn
[1] School of Precision Instrument and Opto-Electronics Engineering, Tianjin University, Tianjin 300072, China
Full list of author information is available at the end of the article

## Abstract

We proposed and demonstrated a flexible, endoscopic, and minimally invasive coherent anti-Raman Stokes scattering (CARS) measurement method for single-cell application, employing a tapered optical fiber probe. A few-mode fiber (FMF), whose generated four-wave mixing band is out of CARS signals, was selected to fabricate tapered optical fiber probes, deliver CARS excitation pulses, and collect CARS signals. The adiabatic tapered fiber probe with a diameter of 11.61 μm can focus CARS excitation lights without mismatch at the focal point. The measurements for proof-of-concept were made with methanol, ethanol, cyclohexane, and acetone injected into simulated cells. The experimental results show that the tapered optical fiber probe can detect carbon-hydrogen (C–H) bond-rich substances and their concentration. To our best knowledge, this optical fiber probe provides the minimum size among probes for detecting CARS signals. These results pave the way for minimally invasive live-cell detection in the future.

**Keywords:** Nonlinear optics, CARS, Tapered optical fiber probe, Raman scattering

## Introduction

The ability to detect intracellular biomolecules and track changes in their concentrations is essential for revealing many prevalent human diseases. For instance, lipids in foam cells play a significant role in determining plaque vulnerability of atherosclerosis [1], and increased de novo lipid synthesis in the cells is a prevalent feature of human malignancies due to the dysregulated metabolic pathways [2]. Detecting the presence and concentration of biomolecules in living cells is essential for studying disease progression and early diagnosis. Coherent anti-Stokes Raman scattering (CARS) is a technique suitable for detecting intracellular biomolecules because of its advantages of chemical selectivity with label-free detection, which results from probing targeted molecular vibrational information [3–5]. CARS is an ideal tool for detecting carbon-hydrogen (C–H) bond-rich biomolecules such as lipids, which show distinct vibrational features in the 2700 $cm^{-1}$ ~ 3200 $cm^{-1}$ of CARS spectrum.

Conventional CARS systems use high numerical aperture (NA) objective lenses to converge the pump light and the Stokes light onto the samples. Such systems achieve the research on highly artificial-isolating individual cells and the quantitative characterization of intracellular biomolecules [6–9]. Although studying single cells is helpful, cells in biological tissues also need to be studied much because it is well known that cells behave quite differently in biological tissues than they do when separated in artificial environments [10]. However, due to the inhomogeneous refractive index (RI) of biological tissues, focused excitation lights are highly scattered and thus cannot reach the cells deep into biological tissues. Moreover, conventional CARS systems require perfect collimation, which is challenging to maintain.

The optical fiber as a laser transmission carrier overcomes some of these restrictions, which can deliver the excitation lights into the sample directly and closely [11]. Owing to the flexibility and portability, the optical fiber is feasible for CARS endoscopic optical detecting cells deep inside tissues. To reduce the sizes of CARS fiber-optic endoscopic probes, micro-scanners and small lens systems are applied to substitute high NA objective lens for focusing excitation lights [12–16]. Although these approaches have been demonstrated in endoscopically detecting the CARS signals deep in the tissue, the millimeter size of these endoscopes prevents them from enabling the non-tissue-destructive, in vivo chemical analysis tools [17]. Advances in optical design, including the use of metamaterials, novel fiber designs, and 3D-printed or freeform optics, enable further miniaturization of CARS optical fiber endoscopic probes [10]. Lombardini et al. inserted a silica microsphere into the output end face of an optical fiber by using a $CO_2$ laser splicer to fabricate a compact CARS optical fiber probe. The silica microsphere served as a lens and focused two output excitation lights on samples [18]. However, the silica microsphere focused the pump light and Stokes light at different positions due to the inherent chromatic aberration, resulting in reduced CARS excitation efficiency. Meanwhile, the sphere shape is difficult to puncture cell membrane and realize intracellular detection, and the process of fixing glass microspheres on the fiber facet is challenging.

The tapered optical fiber probe is a promising solution for these problems. First, the tapered optical fiber probe can be easily fabricated using a homemade or commercial tapering machine. Second, the tapered optical fiber probes will not cause immense damage to cells due to their small size, and the insertion, interrogation and removal processes are time-saving. Furthermore, extracellular events such as cell secretion can be easily detected due to the flexibility of tapered optical fiber probes [19]. The tapered optical fiber probes are widely employed in bioanalysis and cellular-related applications, such as intracellular PH detection [19, 20], cellular protein detection [21, 22] and cancer metabolic compound detection [23]. In addition, the light field with a large intensity gradient emitted by the tapered optical fiber probes can be used for optical fiber tweezers [24]. In other words, the CARS signals detection and optical capture of cell organelles can be integrated into a single tapered optical fiber probe.

In this article, we proposed and demonstrated a flexible endoscopic minimally invasive CARS measurement method with a tapered optical fiber probe, as shown in Fig. 1a. A few-mode fiber (FMF) with generated four-wave mixing (FWM) band out of CARS signals was selected for adiabatic taper optical fiber probe fabrication and fiber deliver line. The adiabatic taper optical fiber probe was used to realize CARS excitation lights

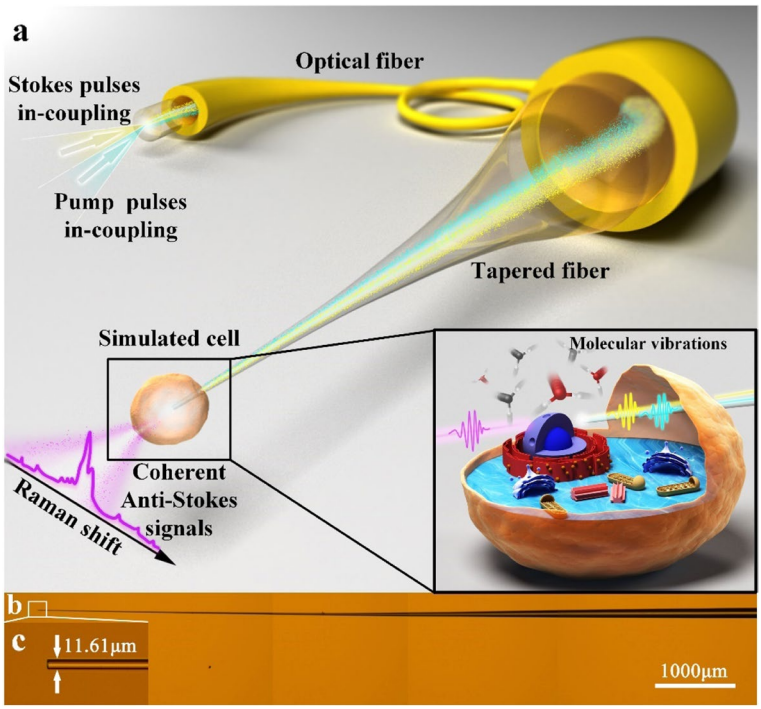


**Fig.1** Principle of a CARS tapered optical fiber probes for single-cell minimally invasive endoscopy. **a** Illustration and **(b)** photography of fabricated device including a tapered fiber tip. **c** Enlarged view of the fiber tip

focusing without mismatch at the focal point. We theoretically analyzed the fraction of the optical power in the fiber, as well as the dispersion and nonlinearity of the optical fiber probe, which indicates that fabricated tapered optical fiber probe with a distal cladding diameter of 11.61 μm enable to deliver and focus the excitation lights, and cause no significant time domain broadening or spectral shift on the excitation pulses. The measurements for proof-of-concept were made with methanol, ethanol, cyclohexane, and acetone injected into simulated cells. The experimental results show that the tapered optical fiber probe can detect C–H bond-rich substances and their concentration. To our best knowledge, the optical fiber probe provides the minimum size among probes for detecting CARS signals. The proposed tapered optical fiber probe is promising to be a non-tissue-destructive, in vivo chemical analysis tool, and opens a significant route towards minimally invasive CARS signals detection of living cells deep in tissues.

## Materials and methods

### CARS excitation and signals collection systems

Our homemade CARS excitation source can generate two chirped ultra-short pulse trains to be utilized as the pump light and the Stokes light, and the CARS excitation source is shown in Fig. 2a. A fiber-based laser source (C-fiber 780, MenloSystems) provides the transform-limited ultrashort pulses with 80.49 fs pulse duration, central wavelength of 780 nm, and spectral bandwidth of 12.82 nm. A liquid crystal variable retarder (LCVR, LCC1113-B, Thorlabs) and a polarization beam splitter (PBS, PBS052, Thorlabs)

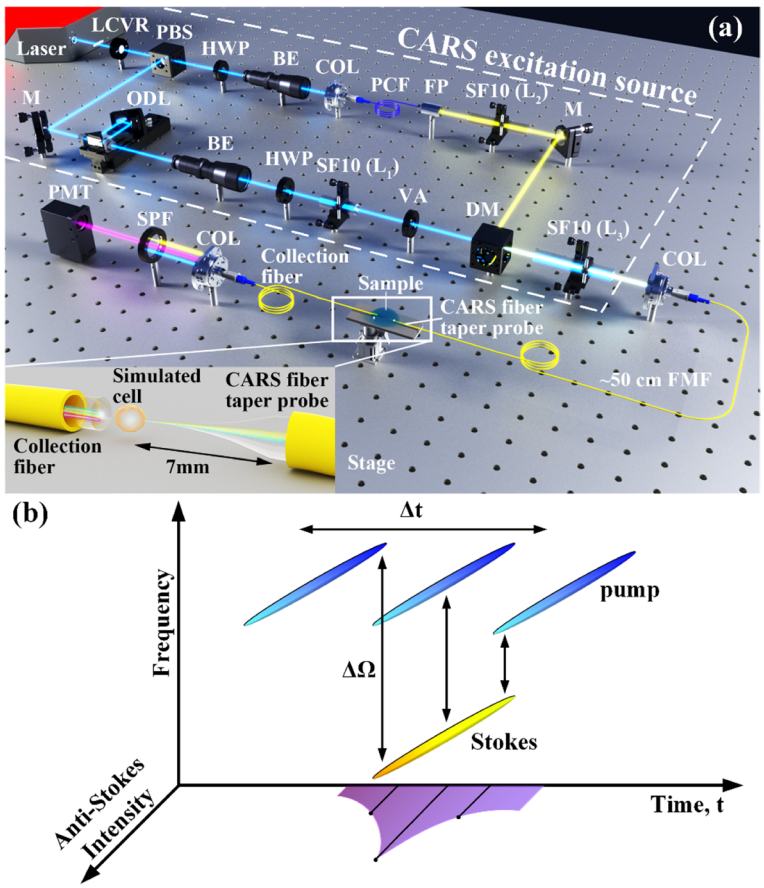


**Fig.2** **a** Schematic diagram of the SSFS-based CARS system with composite wavelength tuning. LCVR: liquid crystal variable retarder, PBS: polarization beam splitter, HWP: half-wave plate, BE: beam expander, FP: fiber-port, PM-PCF: polarization-maintaining photonic crystal fiber, COL: collimator, SF10: SF10 dispersion glass rod, $l_1 = 5$ cm, $l_2 = 15$ cm, $l_3 = 15$ cm, M: mirror, ODL: optical delay line, VA: variable optical attenuator, DM: long-pass dichroic mirror, SPF: short-pass filter, PMT: photomultiplier tubes. **b** Schematic diagram of the frequency difference tuning of the linearly chirped pump and Stokes pulse in spectral focusing by tuning relative time delay

split the femtosecond pulses into two branches with adjustable optical power. The transmitted branch is injected into a 2.81 m polarization-maintaining photonic crystal fiber (PM-PCF, NL-PM-750, NKT Photonics) to generate tunable optical solitons by the soliton self-frequency shift (SSFS) effect. The fundamental soliton, whose wavelength can be tuned to around 1100 nm, passes through a 30 cm SF10 glass rod and serves as the Stokes pulse. The voltage loaded to the LCVR controls the wavelength of the Stokes pulse. The reflected branch passes through an optical delay line (ODL, ODL100/M, Thorlabs) and a 20 cm SF10 glass rod and then acts as the pump pulse. Different lengths of SF10 glass rods inserted in the pump and Stokes light paths exert the same chirp rate on the pump and Stokes pulses to improve the CARS spectral resolution [25]. Eventually, the pump and Stokes pulses are combined by a long-pass dichroic mirror (DM, cut-off wavelength: 900 nm, DMLP900, Thorlabs) and injected into the FMF probe using a collimator (COL, PAF-X-7-B, Thorlabs). The average powers on the sample are ~13 mW for the pump and ~0.7 mW for the Stokes.

The CARS signals collection part collects and detects the generated forward-CARS (F-CARS) signals of samples, including an FMF as collection fiber, a collimator, a short-pass filter (cutoff wavelength 750 nm, FESH0750, Thorlabs), and a photomultiplier tube (PMT, PMM02, Thorlabs). The FMF for CARS signals collection is the same as that used for fabricating tapered fiber. The F-CARS signals of samples are collected by the collection fiber, filtered out from the excitation pulses by the filter, and detected by the PMT. The signal from the PMT is sent to a data acquisition card (NI 6356, National Instruments). The input range is ± 2 V and the ADC resolution is 16 bits. The rise time of PMT in the experiment is 15 μs.

Figure 2b is the schematic diagram of the frequency difference tuning of the linearly chirped pump and Stokes pulse in spectral focusing by tuning relative time delay. The frequency difference between the linearly chirped pulses can be tuned by adjusting the relative optical delay. The SF10 glass rods possess a positive dispersion at excitation pulse frequency. As a result, the leading edge of the pulse is the low-frequency component, and the trailing edge is the high-frequency component. When the high-frequency component of the pump pulse overlaps with the low-frequency component of the Stokes pulse, the frequency difference is the largest, and the high wavenumber CARS signals are excited. When the low-frequency component of the pump pulse overlaps with the high-frequency component of the Stokes pulse, the frequency difference is the smallest, and the low wavenumber CARS signals are excited.

#### CARS tapered optical fiber probe design

The CARS tapered optical fiber probe was fabricated with an FMF. Since the mode field diameter of the FMF is larger than that of the single-mode fiber (SMF), the nonlinear effects in the fiber core of the FMF are weaker. Compared with the step-index FMF and the multimode fiber (MMF), the graded-index FMF supports fewer modes and effectively reduces the impact of intermodal dispersion on CARS excitation lights. Thus, we fabricated a tapered optical fiber probe using a graded-index FMF (FM GI-4, YOFC). The core and cladding diameters of the FMF are 23 μm and 125 μm, respectively. Moreover, the utilization of the graded-index FMF ensures coupling efficiencies of 86% and 78% for the pump light and the Stokes light, respectively. In the case of SMF, the coupling efficiencies are ~ 70% and ~ 60% for the pump light and the Stokes light, respectively. The coupling efficiency is the ratio of the optical power of the excitation light output from the SF10 glass rod of length $L_3$ to the optical power of the excitation light output from the optical fiber. The schematic of the coupling efficiency measurement and the measurement results are shown in Fig. S1.

In addition, the FMF-based tapered fiber probe system can realize CARS excitation delivering and CARS signals detection without background FWM signals. The spectral region from 2700 $cm^{-1}$ to 3200 $cm^{-1}$ represents the 'C–H window' in Raman spectroscopy. In this region, various biological intracellular molecules such as lipids and proteins possess unique characteristics. However, tapered optical fiber probes and fiber delivery systems for CARS detection may encounter the problem of generating FWM signals in the fiber itself at the same spectral region, which cannot be discerned from the useful CARS signals. The FWM signals of a common graded-index MMF are shown as the red solid line in Fig. 3. The FWM signals of the MMF cover from ~ 2700 $cm^{-1}$ to 2900 $cm^{-1}$

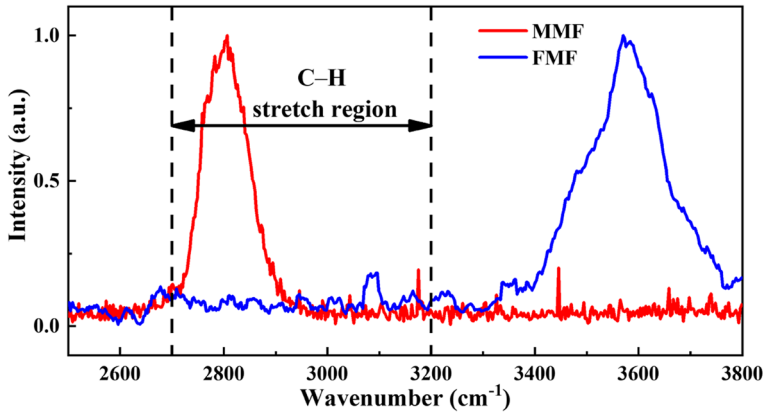


**Fig.3** The FWM signals of MMF cover from ~ 2700 $cm^{-1}$ to 2900 $cm^{-1}$ and interfere with the detection of C–H bond vibrations. The FWM signals of FMF cover from ~ 3400 $cm^{-1}$ to 3800 $cm^{-1}$ and avoid interference to the detection of C–H bond vibrations

and interfere with the detection of C — H bond vibrations. Thus, the fiber probe and fiber delivery systems using such fiber need to suppress or eliminate the generated FWM signals for detection without background noise. Although micro dichroic mirrors, filters and dual-wavelength waveplates can be used to suppress or eliminate FWM signals [13, 16, 26, 27], these spatial optics elements would make the fiber probes bulky, which are incompatible with deep tissue detection in vivo. FMF probes can achieve noise-free CARS detection without filtering elements and reduce the size of probes for the reason that the FWM background of the FMF we used covers from ~ 3400 $cm^{-1}$ to 3800 $cm^{-1}$, as shown in Fig. 3. A possible explanation for the FWM signals of the FMF in the particular band (~ 3400 $cm^{-1}$ to 3800 $cm^{-1}$) is the impurities doped in the fiber. The impurities are added into the core for RI adjustment, and the resonance peaks of some unique impurities are in the range of 3400 $cm^{-1}$ to 3800 $cm^{-1}$, such as boron oxide [28]. Different conditions of fiber processing and preparation may also cause the resonance peaks of the impurities to appear in the range of 3400 $cm^{-1}$ to 3800 $cm^{-1}$. For example, commonly doped impurities within the optical fiber, such as germanium dioxide, can be prepared in various methods. The resonance peak of the hydrothermally-grown germanium dioxide is near 3500 wavenumbers [29].

The optical fiber can be processed into non-adiabatic taper and adiabatic taper. Compared with the non-adiabatic taper, the adiabatic taper we adopted in this work has a smooth taper-transition region, resulting in the main part of the optical energy remaining in the fundamental mode without transferring to higher-order modes, avoiding the effects of intermodal dispersion on the CARS excitation process. As the fiber is tapered down, the light can no longer be confined in the core and is then guided by the cladding-external medium boundary when the difference between the refractive indices (RIs) of the core and the cladding is not large enough. As the fiber is tapered down further, the light can no longer be confined in the fiber and is leaked into the external medium if the diameter of the taper distal is too small, leading to increased insertion loss and reduced CARS excitation efficiency. To choose proper distal cladding diameters, we calculated the fraction η of the optical power confined

in the fiber with different fiber cladding diameters by using the finite-difference time-domain (FDTD) method. The cross-sectional diameter of the FMF cladding is in the range of 4 μm ~ 125 μm. Since the taper length of the adiabatic fiber taper is much larger than the fiber radius, the taper diameter can be considered to decrease approximately linearly. The diameter of the fiber core varies according to the diameter of the tapered cladding with a fixed proportion in the following simulations, and the ratio of the fiber core and the fiber cladding is 23:125. The RI of human tissues is used as the RI of the external medium in the calculation. However, the RIs of human tissues are complicated, and the different tissues possess different RIs. Most human soft tissues have a higher RI than water (1.33), in the range of 1.35 ~ 1.45 [30]. The RIs of water and human adipose tissues (ATs) are used as the RIs of the external mediums, representing the lower and upper limits of the RI of most human soft tissue. Because the RI of ATs is relatively high in the human body. As with any other materials, the RI of human tissue is strongly dependent on the light wavelength. According to the literature [31], the RI of the human ATs at a body temperature of 37 °C was estimated to be 1.455 at 780 nm and 1.452 at 1030 nm.

The calculated η is shown in Fig. 4. The blue solid and dashed lines represent the η at 780 nm and 1030 nm when the RI of water is used as the RI of the external medium. The red solid and dashed lines represent the η at 780 nm and 1030 nm when the RI of ATs is used as the RI of the external medium. When the external medium is water, more than 90% of the energy can be confined in the optical fiber with 4 μm ~ 125 μm cladding diameters. Whereas when the external medium is ATs, more than 20% of the light energy is leaked into the external medium if the cladding diameter is less than 11 μm, resulting in a loss of light energy and a reduction in the excitation efficiency of the CARS signal. When the external medium is Ats, and the fiber diameter is 12 μm, the η is 92.4% at 780 nm and 85.3% at 1030 nm. Considering the fraction of power in the fiber and the strength of the fiber probe, a tapered optical fiber probe with a ~ 12 μm diameter distal is suitable for the CARS tapered optical fiber probe.

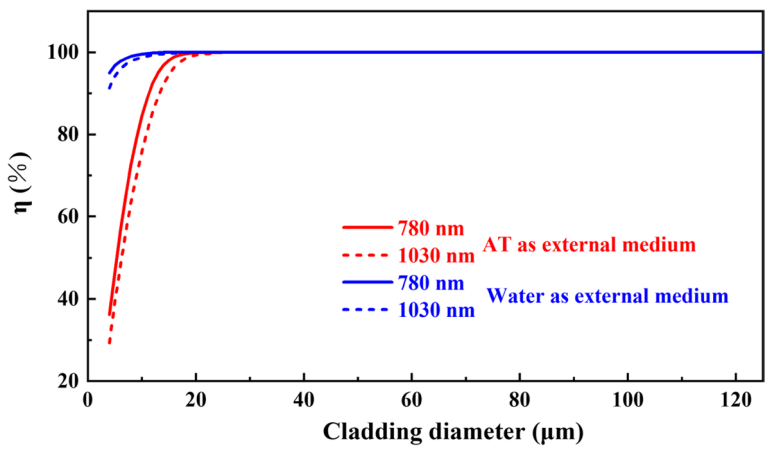


**Fig.4** The calculated results of the fraction of optical power in the fiber η with 4 μm to125 μm cladding diameters. The blue line denotes that the external medium is water, and the red line denotes that the external medium is ATs. The η is 92.4% at 780 nm and 85.3% at 1030 nm when the cladding diameter is 12 μm and the external medium is ATs

### CARS tapered optical fiber probe fabrication

The tapered optical fiber probe was processed using the hydrogen/oxygen flame brushing technique. The tapering process is: firstly, fix the FMF to the fixture and strip the coating layer from the area to be tapered. Secondly, the FMF is continuously heated and stretched by the flame. Thirdly, a fiber splicing system (LDS 2.5, 3SAE) is used to find the thinnest point of tapered fiber, measure the taper waist diameter, and slice it into two parts. The preparation process of tapered optical fiber probe is shown in Fig. S2. The taper length is 7 mm, and the taper diameter is 11.61 μm. The manufactured CARS tapered optical fiber probe has a long pigtail (~ 50 cm) to quickly link with the optical power coupling device and facilitate operation. The fabricated tapered optical fiber probe is shown in Fig. 1b.

### Calculation of the effect of tapered optic fiber probes on CARS excitation pulses

To analyze and estimate the time domain broadening and spectral shift caused by the tapered optical fiber, we calculated the dispersion and nonlinearity of the FMF with 4 μm ~ 125 μm cross-sectional cladding diameters, and the results are shown in Fig. 5a. The red solid line and the dashed red line represent the dispersion at 780 nm and

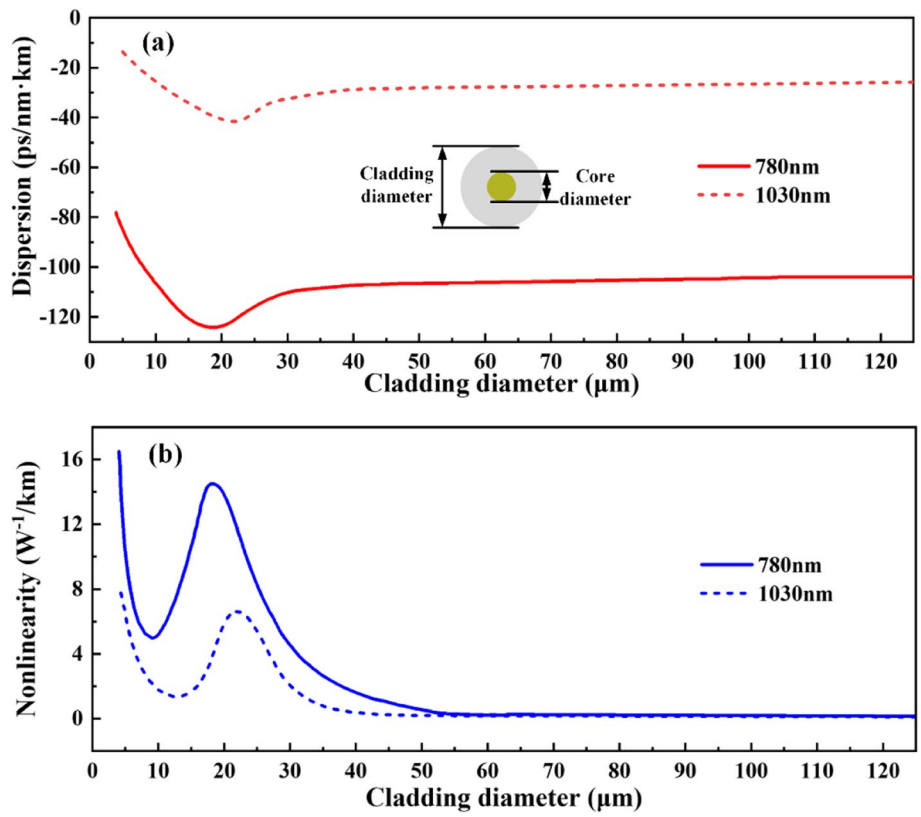


**Fig.5** **a** Calculated dispersion of optical fiber with 4 μm ~ 125 μm cladding diameter. The dispersion at 780 nm and 1030 nm reaches minimum values of -124.04 ps/nm·km and -41.44 ps/nm·km at 18 μm and 21 μm cladding diameters, respectively. **b** Calculated nonlinearity of optical fiber with 4 μm ~ 125 μm cladding diameter. The nonlinearity at 780 nm and 1030 nm reaches maximum values of 14.52 $W^{-1}$/km and 6.66 $W^{-1}$/km at 19 μm and 22 μm cladding diameters respectively, and reaches minimum values of 4.98 $W^{-1}$/km and 1.38 $W^{-1}$/km at 9 μm and 12 μm cladding diameters respectively

1030 nm, respectively. As a function of cladding diameter, the dispersion at 780 nm follows a similar trend to that at 1030 nm. Firstly, the dispersion at 780 nm and 1030 nm steadily remains -103.91 ps/nm·km and -25.73 ps/nm·km when the cladding diameter is larger than 30 μm, respectively. Secondly, the dispersion gradually decreases as the cladding diameter decreases. The dispersion at 780 nm reaches a minimum of -124.04 ps/nm·km with a cladding diameter of 18 μm and at 1030 nm reaches a minimum of -41.44 ps/nm·km with a cladding diameter of 21 μm. Thirdly, the dispersion increases as the cladding diameter further decreases due to the increased proportion of light energy transmitted in the cladding and the larger diameter of the optical fiber mode field. In Fig. 5b, the blue solid line and the dashed blue line represent the nonlinearity at 780 nm and 1030 nm, respectively. Firstly, the nonlinearity at 780 nm and 1030 nm constantly remains 0.16 $W^{-1}$/km and 0.12 $W^{-1}$/km, and then gradually increases. The nonlinearity at 780 nm reaches a maximum of 14.52 $W^{-1}$/km with a 19 μm cladding diameter and at 1030 nm reaches a maximum of 6.66 $W^{-1}$/km with a 22 μm cladding diameter. Secondly, the nonlinearity decreases as the cladding diameter decreases. The nonlinearity at 780 nm reaches a minimum of 4.98 $W^{-1}$/km when the cladding diameter is 9 μm and 1.38 $W^{-1}$/km at 1030 nm when the cladding diameter is 12 μm. Thirdly, as the cladding diameter further decreases, the nonlinearity turns to increase. As the cladding diameter decreases, the nonlinearity first increases, then decreases, and finally increases again because the propagation mode transfers from the core mode to the cladding. The light spreads and redistributes in the cladding in the process, leading to a change of the effective mode area and ultimately to a change in the nonlinearity.

The general nonlinear Schrödinger equation (GNLSE) was used to numerically analyze the variation of the time domain broadening and the spectral shift of the ultrashort pulses through the tapered optical fiber probe. The taper length is 7 mm, and the taper diameter is 11.61 μm. We use the calculated dispersion and nonlinearity with 11.61 μm ~ 125 μm cladding diameter in Fig. 5 to approximate the fiber's characteristics at arbitrary positions along the fiber. The calculated results are shown in Fig. 6. The red solid and dashed lines represent the time domain broadening at 780 nm and 1030 nm, respectively. According to the calculated results, the time domain broadening increases with the time width of the incident ultrashort pulses, the overall broadening ratio is low (< 1.02). Because the length of the tapered optical fiber probe used is 7 mm and the dispersion and the nonlinearity only vary significantly when the cladding diameter is less than 20 μm. Therefore, the time domain broadening of the ultrashort pulses transmitted in the tapered optical fibered probe is mainly caused by dispersion. The blue solid and dashed lines in Fig. 6 represent the spectral shift for 780 nm and 1030 nm, respectively. The solid and dashed lines overlap, and both remain at zero as the time domain width of ultra-short pulse increases. When the ultrashort pulse is transmitted in the tapered optical fiber probe, the overall nonlinear coefficient of the tapered optical fiber probe is low. The tapered optical fiber probe does not bring a significant spectral shifting to the ultrashort pulses because the interaction length of the ultrashort pulse and the high nonlinearity part of the tapered optical fiber probe is limited.

A miniaturized, flexible, and robust fiber probe is fabricated without bulky optical or mechanical parts. Benefiting from the all-fiber design, the fiber probe can be recycled after disinfection and sterilization.

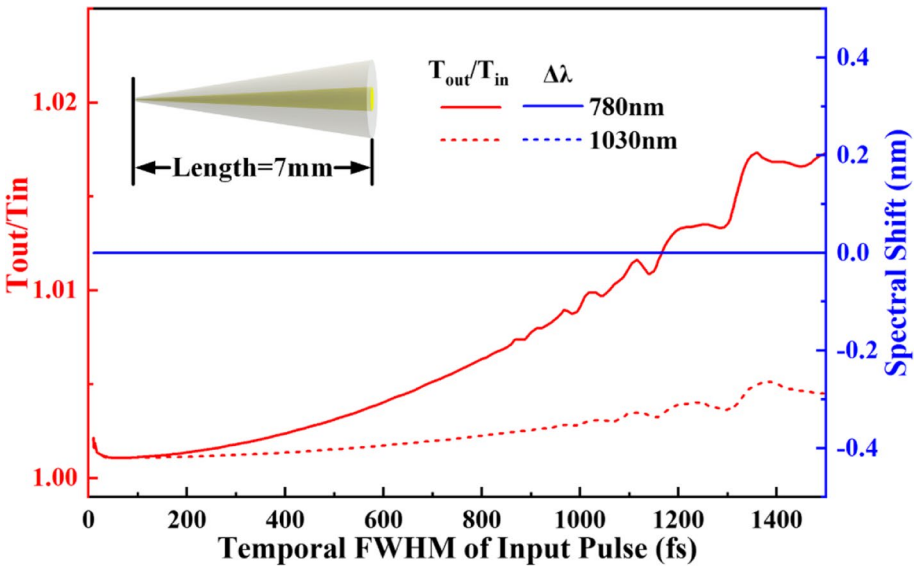


**Fig.6** The calculated time domain broadening and the spectral shift of ultrashort pulses with different pulse widths transmitted by a 7 mm tapered optical fiber probe. The total time domain broadening ratio is < 1.02 for 780 nm pulses and < 1.005 for 1030 nm pulses

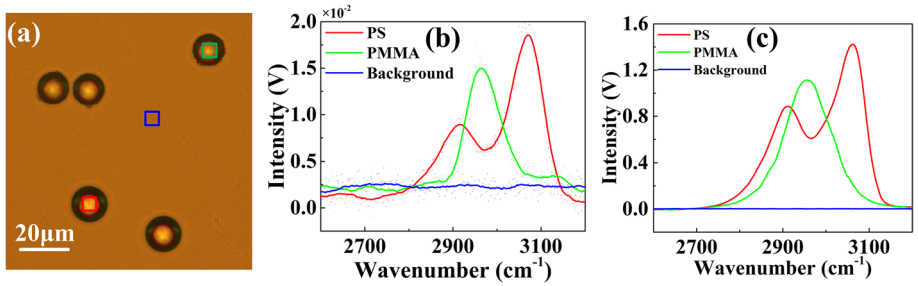


**Fig.7** **a** Microscope image of PS microsphere and PMMA microsphere samples, the blue, red and green squares represent the slide background, PS microsphere, and PMMA microsphere, respectively. **b** CARS signals detected by the optical fiber probe and **c** free-space elements. The blue, red and green solid lines represent the signals of slide background, PS microsphere, and PMMA microsphere, respectively

## Results

We first demonstrated the capability of distinguishing different Raman spectra of our tapered optical fiber probe by using two microspheres samples. One sample was 15-μm polystyrene microspheres (PS, PSMS-1.07, Cospheric), and another sample was 15-μm polymethyl methacrylate microspheres (PMMA, PMPMS-1.2, Cospheric). Figure 7a shows the microscopic image of the PS and the PMMA microspheres. Both microspheres were deposited on the slides. The measured CARS spectra were obtained for dark background (the blue square in Fig. 7a), PMMA microspheres (the green square in Fig. 7a) and PS microsphere (the red square in Fig. 7a), and the results are plotted with the same color code as in Fig. 7b. The Raman resonance peaks at 2912 $cm^{-1}$ and 3064 $cm^{-1}$ for the PS microspheres, and 2953 $cm^{-1}$ for the PMMA microspheres are visible. These experimental results demonstrate the ability of tapered optical fiber probes to perform chemical-specific detection by detecting CARS spectra.

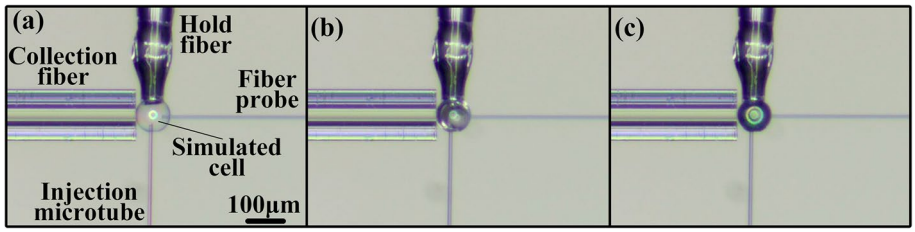


**Fig.8** **a** Physical micrograph of tapered optical fiber probe probing a simulated cell. **b** The liquid was being injected into the simulated cell. **c** Liquid-filled simulated cell

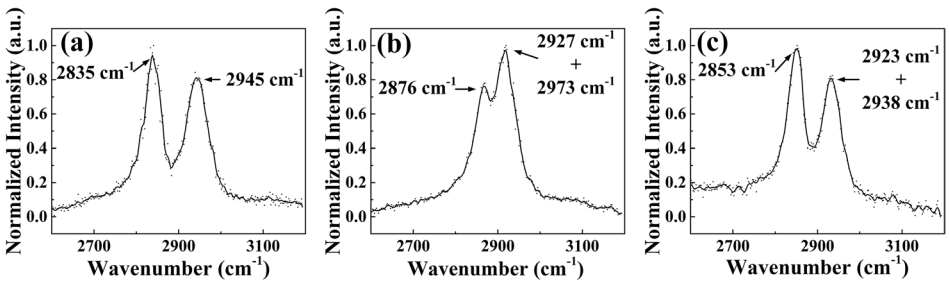


**Fig.9** CARS spectra of **a** methanol, **b** ethanol, and **c** cyclohexane detected by CARS fiber probe

For reference, the objective-based free-space elements were used to deliver and focus the CARS excitation lights to the samples, and collect the F-CARS signals. The detected CARS spectra are shown in Fig. 7c. The CARS spectral peak positions of PS and PMMA microspheres are consistent with CARS spectra obtained by the tapered fiber probe. The two CARS signals are similar, demonstrating that the intermodal dispersion in FMF does not affect the properties of the fiber probe.

Next, we moved to simulated cells to demonstrate the capability for single-cell endoscopic detection. Here a hollow glass microbubble fixed on the hold fiber served as simulated cells. The diameter of the hollow glass microbubble used in the experiment is 75 μm, which is close to some interesting cells, such as the macrophage foam cells that cause atherosclerosis and hepatocellular carcinoma cells [32–34]. A microtube with a diameter of 12 μm was connected to a syringe pump. The microtube was manipulated by a three-dimensions (3D) micromanipulator so that the different liquids simulating cytoplasm could be readily injected into the simulated cell. The tapered optical fiber probe mounted on another 3D micromanipulator was carefully inserted into the simulated cell and delivered the excitation lights. The F-CARS signals were collected by the collection fiber and detected by the PMT. The physical micrograph of tapered optical fiber probe probing a simulated cell is shown in Fig. 8a. Figure 8b and c show that the simulated cell was being filled with liquid and had been filled with liquid, respectively.

Figure 9a shows the measured CARS spectra of the methanol injected into the simulated cell, and the two peaks corresponding to the Raman resonance at 2835 $cm^{-1}$ and 2945 $cm^{-1}$ are successfully detected. Figure 9b shows the CARS spectra of injected ethanol in the microbubble. Due to the limited resonance spectrum resolution of the CARS system and the weak energy of the Raman resonance peak of ethanol at

2973 $cm^{-1}$, the Raman resonance peaks at 2927 $cm^{-1}$ and 2973 $cm^{-1}$ are displayed in one peak. Figure 9c shows the CARS spectra of injected cyclohexane. The first peak signals correspond to the Raman resonance of cyclohexane at 2853 $cm^{-1}$, and the second peak signals contain the Raman resonance at 2923 $cm^{-1}$ and 2938 $cm^{-1}$.

Overall, Fig. 9 shows that the tapered optical fiber probe can detect CARS signals of the liquid samples in the simulated cell, demonstrating its applicability for a CARS endoscopic detecting setup. The tapered optical fiber probe can measure Raman resonance spectra with a resolution of ~ 50 $cm^{-1}$.

In addition to measuring samples qualitatively in simulated cells, the tapered optical fiber probe can also be used for detecting the local concentration of a specific molecule in a cell, which is helpful for tracking molecule uptake and metabolism. To demonstrate the quantitative detection capability of the tapered optical fiber probe, we injected acetone with different concentrations into the simulated cell. The CARS signals strength of $CH_3$ mode provides, in theory, a handle for detecting acetone concentration. The intensity of the CARS signals corresponding to different acetone concentrations is shown in Fig. 10a. We calibrate the CARS intensity measured at 2921 $cm^{-1}$ as a function of acetone concentration in water, and the results are shown in Fig. 10b. A linear fitting is executed in the concentration range of 50 ~ 100%, and the calculated measurement resolution is 0.113% (16 mM), as shown in Fig. 10b. The dependence between CARS signals and acetone concentration is approximately quadratic. Such phenomena are due to the coherence property of CARS, that is, the quadratic dependence of signals intensity on the number of vibrational modes [35]. The insert in Fig. 10a shows the CARS spectra of 10 v/v% acetone and water, demonstrating the ability of the tapered optical fiber probe to discriminate between $CH_3$ and OH bonds in the solution.

## Conclusion

In conclusion, we proposed and demonstrated a flexible, endoscopic, and minimally invasive CARS measurement with a tapered optical fiber probe for single-cell application. An adiabatic taper optical fiber probe was used to realize CARS excitation light focusing without mismatch at the focal point. An FMF with generated FWM band in 3400 $cm^{-1}$ ~ 3800 $cm^{-1}$, which is out of CARS signals band (2700 $cm^{-1}$ ~ 3200 $cm^{-1}$),

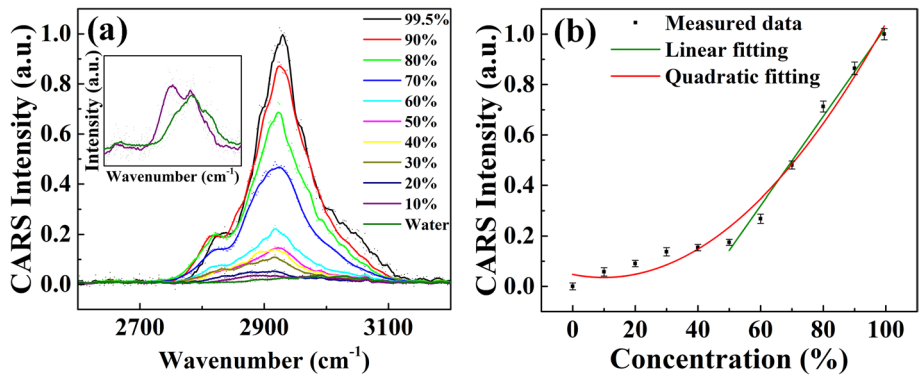


**Fig.10** **a** CARS spectra of acetone with different volume fractions in water. Inset: CARS spectra of 10 v/v% acetone and water. **b** Relative CARS intensity at 2921 $cm^{-1}$ for increasing volume fractions of acetone in water

is selected for adiabatic taper optical fiber probe fabrication, CARS excitation lights delivery, and CARS signals collection. We theoretically analyzed the fraction of the optical power in the fiber, dispersion and nonlinearity of optical fiber probe, which indicated that fabricated tapered optical fiber probes with 11.61 μm distal cladding diameter enable to deliver and focus the excitation light effectively and cause no significant time domain broadening or spectral shift on the excitation pulses. The measurements for proof-of-concept were made with methanol, ethanol, cyclohexane, and acetone injected into simulated cells. We believe that the fiber probe opens up exciting perspectives for intraoperative label-free detecting for real-time histopathology diagnosis.

**Abbreviations**

CARS: Coherent anti-Raman Stokes scattering; FMF: Few-mode fiber; C–H: Carbon-hydrogen; NA: Numerical aperture; RI: Refractive index; FWM: Four-wave mixing; LCVR: Liquid crystal variable retarder; PBS: Polarization beam splitter; HWP: Half-wave plate; BE: Beam expander; VA: Variable optical attenuator; PM-PCF: Polarization-maintaining photonic crystal fiber; SSFS: Soliton self-frequency shift; ODL: Optical delay line; DM: Dichroic mirror; FP: Fiber-port; F-CARS: Forward-CARS; SPF: Short-pass filter; PMT: Photomultiplier tube; SMF: Single-mode fiber; MMF: Multimode fiber; RIs: Refractive indices; FDTD: Finite-difference time-domain; ATs: Adipose tissues; GNLSE: General nonlinear Schrödinger equation; PS: Polystyrene; PMMA: Polymethyl methacrylate; 3D: Three-dimensions.

## Supplementary Information

The online version contains supplementary material available at https://doi.org/10.1186/s43074-022-00058-0.

**Additional file 1: Fig. S1.** Schematic diagram of measuring coupling efficiency of the fiber. The coupling efficiency is the ratio of the optical power P2 of the excitation light output from the flat fiber end face to the optical power P1 of the excitation light output from the SF10 glass rod of length L3. The optical power is detected by a power meter (S145C+PM100D, Thorlabs).

**Additional file 2: Fig. S2**. The preparation process of tapered optical fiber probe.

**Acknowledgements**

Not applicable at this moment.

**Authors' contributions**

T.W. conceived the study and designed the experiments, and performed the optical experiments. P.N. and Y.L. provided useful advice. J.J., K.L., S.W., and T.L. supervised the project. All authors contributed to the discussion and manuscript writing. The authors read and approved the final manuscript.

**Funding**

This work was supported by the National Natural Science Foundation of China (NO. 61735011), National Key Scientific Instrument and Equipment Development Projects of China (NO. 2013YQ030915), State Key Laboratory of Information Photonics and Optical Communications (NO. 2021KFKT006), Tianjin Talent Development Special Plan for High Level Innovation and Entrepreneurship Team, and the first rank of Tianjin 131 Innovation Talent Development Program.

**Availability of data and materials**

The data and the relevant methods are available on request from the corresponding authors.

## Declarations

**Ethics approval and consent to participate**

There is no ethics issue for this paper.

**Consent for publication**

All authors agreed to publish this paper.

**Competing interests**

There are no competing interests for this paper.

**Author details**

[1]School of Precision Instrument and Opto-Electronics Engineering, Tianjin University, Tianjin 300072, China. [2]Key Laboratory of Opto-Electronics Information Technology, Ministry of Education, Tianjin University, Tianjin 300072, China. [3]Tianjin Optical Fiber Sensing Engineering Center, Institute of Optical Fiber Sensing of Tianjin University, Tianjin University, Tianjin 300072, China.

Received: 4 January 2022 Accepted: 18 April 2022
Published online: 24 April 2022

**References**

1. Kellner-Weibel G, et al. Crystallization of Free Cholesterol in Model Macrophage Foam Cells. Atertio Thromb Vasc Biol. 1999;19:1891–8. https://doi.org/10.1161/01.ATV.19.8.1891.
2. Yue S, et al. Cholesteryl ester accumulation induced by PTEN loss and PI3K/AKT activation underlies human prostate cancer aggressiveness. Cell Metab. 2014;19:393–406. https://doi.org/10.1016/j.cmet.2014.01.019.
3. Zumbusch A, Holtom GR, Xie XS. Three-dimensional vibrational imaging by coherent anti-Stokes Raman scattering. Phys Rev Lett. 1999;82:4142. https://doi.org/10.1103/PhysRevLett.82.4142.
4. Cheng JX, Xie XS. Coherent anti-Stokes Raman scattering microscopy: instrumentation, theory, and applications. J Phys Chem B. 2004;108:827–40. https://doi.org/10.1021/jp035693v.
5. Yue S, Cheng JX. Deciphering single cell metabolism by coherent Raman scattering microscopy. Curr Opin Chem Biol. 2016;33:46–57. https://doi.org/10.1016/j.cbpa.2016.05.016.
6. Lee YJ, et al. Quantitative, label-free characterization of stem cell differentiation at the single-cell level by broadband coherent anti-Stokes Raman scattering microscopy. Tissue Eng, Part C. 2014;20:562–9. https://doi.org/10.1089/ten.tec.2013.0472.
7. Di Napoli C, et al. Quantitative spatiotemporal chemical profiling of individual lipid droplets by hyperspectral CARS microscopy in living human adipose-derived stem cells. Anal Chem. 2016;88:3677–85. https://doi.org/10.1021/acs.analchem.5b04468.
8. Hofemeier AD, et al. Label-free nonlinear optical microscopy detects early markers for osteogenic differentiation of human stem cells. Sci Rep. 2016;6:26716. https://doi.org/10.1038/srep26716.
9. Capitaine E, et al. Fast epi-detected broadband multiplex CARS and SHG imaging of mouse skull cells. Biomed Opt Express. 2018;9:245–53.
10. Untracht GR, Karnowski K, Sampson DD. Imaging the small with the small: Prospects for photonics in micro-endomicroscopy for minimally invasive cellular-resolution bioimaging. APL Photonics. 2021;6: 060901.
11. Wang H, Huff TB, Cheng JX. Coherent anti-Stokes Raman scattering imaging with a laser source delivered by a photonic crystal fiber. Opt Lett. 2006;31:1417–9. https://doi.org/10.1364/OL.31.001417.
12. Balu M, Liu GJ, Chen ZP, Tromberg BJ, Potma EO. Fiber delivered probe for efficient CARS imaging of tissues. Opt Express. 2010;18:2380–8. https://doi.org/10.1364/OE.18.002380.
13. Smith B, et al. Portable, miniaturized, fibre delivered, multimodal CARS exoscope. Opt Express. 2013;21:17161–75. https://doi.org/10.1364/OE.21.017161.
14. Chen X, Xu X, McCormick DT, Wong K, Wong ST. Multimodal nonlinear endo-microscopy probe design for high resolution, label-free intraoperative imaging. Biomed Opt Express. 2015;6:2283–93. https://doi.org/10.1364/BOE.6.002283.
15. Lukić A, et al. Fiber probe for nonlinear imaging applications. J Biophotonics. 2016;9:138–43.
16. Lukic A, et al. Endoscopic fiber probe for nonlinear spectroscopic imaging. Optica. 2017;4:496–501. https://doi.org/10.1364/OPTICA.4.000496.
17. Kim SH, et al. Multiplex coherent anti-stokes Raman spectroscopy images intact atheromatous lesions and concomitantly identifies distinct chemical profiles of atherosclerotic lipids. Circul Res. 2010;106:1332–41. https://doi.org/10.1161/CIRCRESAHA.109.208678.
18. Lombardini, A. *et al.* High-resolution multimodal flexible coherent Raman endoscope. Light Sci Appl. 2018;**7**:1–8. https://doi.org/10.1038/s41377-018-0003-3.
19. Wang J, et al. SERS-active fiber tip for intracellular and extracellular pH sensing in living single cells. Sens Actuators B: Chem. 2019;290:527–34. https://doi.org/10.1016/j.snb.2019.03.149.
20. Yang Q, et al. Fiber-optic-based micro-probe using hexagonal 1-in-6 fiber configuration for intracellular single-cell pH measurement. Anal Chem. 2015;87:7171–9. https://doi.org/10.1021/acs.analchem.5b01040.
21. Kasili PM, Song JM, Vo-Dinh T. Optical sensor for the detection of caspase-9 activity in a single cell. J Am Chem Soc. 2004;126:2799–806. https://doi.org/10.1021/ja037388t.
22. Liang F, et al. Direct tracking of amyloid and tau dynamics in neuroblastoma cells using nanoplasmonic fiber tip probes. Nano Lett. 2016;16:3989–94. https://doi.org/10.1021/acs.nanolett.6b00320.
23. Zheng XT, Yang HB, Li CM. Optical detection of single cell lactate release for cancer metabolic analysis. Anal Chem. 2010;82:5082–7. https://doi.org/10.1021/ac100074n.
24. Liu Z, Guo C, Yang J, Yuan L. Tapered fiber optical tweezers for microscopic particle trapping: fabrication and application. Opt Express. 2006;14:12510–6. https://doi.org/10.1364/OE.14.012510.
25. Cole R, Slepkov A. Interplay of pulse bandwidth and spectral resolution in spectral-focusing CARS microscopy. JOSA B. 2018;35:842–50. https://doi.org/10.1364/JOSAB.35.000842.
26. Wang Z, et al. Coherent anti-Stokes Raman scattering microscopy imaging with suppression of four-wave mixing in optical fibers. Opt Express. 2011;19:7960–70. https://doi.org/10.1364/OE.19.007960.
27. Wang Z, et al. Use of multimode optical fibers for fiber-based coherent anti-Stokes Raman scattering microendoscopy imaging. Opt Lett. 2011;36:2967–9. https://doi.org/10.1364/OL.36.002967.
28. Kipcak A, Senberber F, Derun EM, Piskin S. Evaluation of the magnesium wastes with boron oxide in magnesium borate synthesis. J Mater Metall Eng. 2012;6:610–4. https://doi.org/10.5281/zenodo.1056553.
29. Armand P, Lignie A, Beaurain M, Papet P. Flux-grown piezoelectric materials: application to α-quartz analogues. Curr Comput-Aided Drug Des. 2014;4:168–89. https://doi.org/10.3390/cryst4020168.
30. Khan R, Gul B, Khan S, Nisar H, Ahmad I. Refractive index of biological tissues: review, measurement techniques, and applications. Photodiagn Photodyn Ther. 2021;33: 102192. https://doi.org/10.1016/j.pdpdt.2021.102192.

31. Yu YI, Lazareva EN, Tuchin VV. Refractive index of adipose tissue and lipid droplet measured in wide spectral and temperature ranges. Appl Opt. 2018;57:4839–4848. https://doi.org/10.1364/AO.57.004839.
32. Gerrity RG. The role of the monocyte in atherogenesis: I. Transition of blood-borne monocytes into foam cells in fatty lesions. Am J Pathol. 1981;103:181–90.
33. Takaku M, et al. An in vitro coculture model of transmigrant monocytes and foam cell formation. Atertio Thromb Vasc Biol. 1999;19:2330–9.
34. Li Y, et al. Establishment of cell clones with different metastatic potential from the metastatic hepatocellular carcinoma cell line MHCC97. World J Gastroenterol. 2001;7:630–6. https://doi.org/10.3748/wjg.v7.i5.630.
35. Cheng JX, Potma EO, Xie SX. Coherent anti-Stokes Raman scattering correlation spectroscopy: probing dynamical processes with chemical selectivity. J Phys Chem A. 2002;106:8561–8. https://doi.org/10.1021/jp025774b.

## Publisher's Note